RESEARCH ARTICLE

Rising Stars

ADVANCED MATERIALS TECHNOLOGIES

www.advmattechnol.de

Machine Learning Enabled Design and Optimization for 3D-Printing of High-Fidelity Presurgical Organ Models

Eric S. Chen, Alaleh Ahmadianshalchi, Sonja S. Sparks, Chuchu Chen, Aryan Deshwal, Janardhan R. Doppa, and Kaiyan Qiu**

The development of a general-purpose machine learning algorithm capable of quickly identifying optimal 3D-printing settings can save manufacturing time and cost, reduce labor intensity, and improve the quality of 3D-printed objects. Existing methods have limitations which focus on overall performance or one specific aspect of 3D-printing quality. Here, for addressing the limitations, a multi-objective Bayesian Optimization (BO) approach which uses a general-purpose algorithm to optimize the black-box functions is demonstrated and identifies the optimal input parameters of direct ink writing for 3D-printing different presurgical organ models with intricate geometry. The BO approach enhances the 3D-printing efficiency to achieve the best possible printed object quality while simultaneously addressing the inherent trade-offs from the process of pursuing ideal outcomes relevant to requirements from practitioners. The BO approach also enables us to effectively explore 3D-printing inputs inclusive of layer height, nozzle travel speed, and dispensing pressure, as well as visualize the trade-offs between each set of 3D-printing inputs in terms of the output objectives which consist of time, porosity, and geometry precisions through the Pareto front.

1. Introduction

3D-printing has seen growing usage and innovation in recent years, allowing both researchers and industrial engineers to quickly convert customized designs to products,[1,2] which are time-consuming and expensive to achieve through traditional manufacturing. Many functional devices in different disciplines have been designed and manufactured through 3D-printing, including presurgical organ models,[3,4] sensors,[5–7] biological structures,[8] bone implantations,[9,10] batteries,[11,12] wearable devices,[13,14] assistive-devices,[15,16] and aerospace parts.[17,18] Among the 3D-printing approaches, direct ink writing (DIW)[19] can print a broad range of customizable ink materials, enabling a wide spectrum of potential applications ranging from surgical rehearsal[3,4] and health monitoring[5–7] to shape changes with external stimuli,[20,21] thermal/electric conduction, and strength resistance.[22,23] DIW stands as the most versatile form of 3D-printing and involves the precise extrusion of a material compound, layer by layer, for structures requiring complex geometries.[24,25]

Despite the rapid emergence of novel applications in 3D-printing, the process of selecting appropriate parameters for 3D-printing remains a labor-intensive and inefficient process. This pertains to pivotal aspects such as identifying the optimal material composition or printer configuration, as well as mitigating defects that occur during printing.[26] Specifically, there are several considerable difficulties when trying to optimize the critical parameters of 3D-printing to closely replicate real-world object models by manipulating variables such as layer height, dispensing pressure, and nozzle travel speed. These challenges are particularly evident when fine-tuning the overall print quality, as several key issues arise in this context. First, the vast range of available 3D-printing settings makes traditional trial-and-error experimentation impractical as the sheer number of potential combinations is overwhelming, and each trial is time and cost ineffective. Second, assessing various 3D-printing design configurations against multiple quality criteria involves expensive test prints and complex geometric calculations. Third, 3D-printing settings must conform to stringent quality constraints, such as the precision of shape and its porosity, necessitating laborious verification processes. Lastly, the ideal 3D-printing settings often vary depending on the desired output, whether it is a high-detail figurine or a rapid prototype.

Existing methods for optimizing 3D-printing parameters have limitations. They often concentrate on optimizing the printing's overall performance or focus on one specific aspect of printing quality.[27] These methods primarily rely on experimental

E. S. Chen, S. S. Sparks, C. Chen, K. Qiu
School of Mechanical and Materials Engineering
Washington State University
Pullman, Washington 99164, USA
E-mail: kaiyan.qiu@wsu.edu

A. Ahmadianshalchi, A. Deshwal, J. R. Doppa
School of Electrical Engineering and Computer Science
Washington State University
Pullman, Washington 99164, USA
E-mail: jana.dopp@wsu.edu

The ORCID identification number(s) for the author(s) of this article can be found under https://doi.org/10.1002/admt.202400037

DOI: 10.1002/admt.202400037

data from previous 3D-printing configurations documented in the literature[28] or research records. However, they tend to overlook variations in the print quality due to differences in printing approaches, material types, and object geometries by focusing on just one of these aspects. For instance, data from prior 3D-printing configurations for a cubical shape cannot be readily applied to 3D-printing of a spherical object, given the significant differences in printing parameter settings. Consequently, there is a need for a general-purpose algorithm capable of identifying optimal 3D-printing settings to achieve the best possible printed object quality, regardless of the printing type, material, or shape in use.

Incorporation of data-driven artificial intelligence and its subset, machine learning (ML), enables us to expedite the process of refining 3D-printing parameter settings by reducing time and cost.[29] A multi-objective optimization (MOO) algorithm has been used to discover optimal material formulations and their individual trade-offs in 3D-printing.[30] In other works, MOO algorithms have also been used to improve print quality, printing performance, and the mechanical properties of 3D-printed objects.[31–33] For biomaterial inks used in 3D-printing,[34] random forest and deep learning algorithms, which are branches of ML, have successfully predicted the printability of varying bio-compounds.[35] Other ML methods including convolutional neural network models, a form of deep learning, have commonly been used for defect detection and correction for 3D-printed objects due to their ability to automatically learn and recognize specific features, such as pores or warped areas, through pattern recognition within image datasets.[36–38] In metal additive manufacturing, analysis of feature characterization for fabricating desired microstructures[39] and melt pool[40] characteristics has been achieved with ML identification techniques. Moreover, reinforcement learning has been applied to DIW for achieving optimal material deposition through modifying velocity and printing path inputs via a reward-based system.[41]

Bayesian optimization (BO),[42,43] is a powerful ML technique for optimizing complex, expensive, black-box objective functions. It is often used in various science and engineering domains. Some examples of BO usage in engineering include optimizing analog circuit design,[44,45] aircraft design,[46] and nanoporous material discovery.[47] Recently, BO for optimizing a set of parameters through evaluating objective functions, has been adapted for material science and 3D-printing.[29,48] Fused deposition modeling (FDM), a heated extrusion-based form of 3D-printing that primarily uses plastic filaments, has seen usage of an autonomous robot to find optimal printer configurations using BO for desired single-layer feature accuracy.[49] However, existing research on applying ML techniques to multi-layered features is still limited, especially within the realm of DIW. Most applications aim for simple, single-layer prints with basic structures and employ a single-objective optimization algorithm for individual attributes such as geometry or porosity. For instance, a set of printing inputs with the most optimal time output may suffer in geometry due to an exceedingly quick nozzle travel speed, though the inverse can also hold true. Thus, it is important that multiple input and output criteria are to be considered for optimizing the 3D-printing process, as each property indirectly affects each other.

In this work, we designed a principled methodology aimed at identifying the optimal DIW 3D-printing input parameters for manufacturing different presurgical organ (prostate and kidney) models, with the application of multi-objective BO[50] designed for optimizing black-box functions that are expensive to evaluate in terms of physical resources. We seek to enhance the efficiency of the DIW process while concurrently addressing the inherent trade-offs that arise in pursuit of ideal outcomes. BO, unlike other ML techniques, enabled us to effectively explore the input search space regarding possible parameters of layer height, nozzle travel speed, and dispensing pressure. BO also enabled the visualization of trade-offs between each set of printing inputs in terms of the output objectives comprising of time, porosity, positive precision, and negative precision through the Pareto front. The Pareto front is a set of optimal trade-off solutions or input parameters that are dominant in their own regard due to an advantage in a single or multiple output objective values. We apply the BO algorithm to multi-layered 3D-printed organ models with intricate geometry, inclusive of a patient-specific prostate model and a general-purpose kidney model, which introduces a biomedical aspect that can be further explored. Our approach yields a diverse set of DIW printing settings that strike a favorable balance between all the objectives relevant to the practitioners' requirements.

2. Results and Discussion

Our methodology for ML assisted 3D-printing is a four-step recursive process, as depicted in **Figure 1**. The process consists of the following four iterative steps, including 1) inputs generation through a BO algorithm: this step includes BO algorithm development and generation of different input parameters for printing settings (layer height, nozzle travel speed, and dispensing pressure); 2) 3D-printing process: this step applies customized polymeric inks and the DIW process for manufacturing presurgical organ models (prostate and kidney); 3) imaging process: this step detects and generates the digital geometries of the 3D-printed organ models for a geometric assessment; and 4) outputs evaluation: this step evaluates the output objective values from the 3D-printed organ models, including time for 3D-printing, porosity of the model (by mass), and geometrical precision.

We define the input space in three dimensions, specifically including the parameters for layer height, nozzle travel speed, and dispensing pressure. The respective ranges for each input dimension are as follows: layer height [0.26 mm, 0.61 mm], dispensing pressure [98 kPa, 449 kPa], and nozzle travel speed [4 mm $^{-1}$s, 15 mm $^{-1}$s]. The preliminary step started with randomly generating four sets of input parameters (non-inclusive to the iterations), and these generated values were based on our early data for printing parameters using a customized silicone ink. The early data were obtained through printing small cylinders (10 mm diameter x 10 mm height) with acceptable geometries using the customized silicone ink. The components of the silicone ink in this study mainly included an active agent (silicone sealant) and bulking agent (silicone grease) with a weight ratio of 8:4.5, and the ink showed a Young's modulus of 407.5 kPa (**Figure 2a**), which is close to the biological organ tissue.[51] These four input sets served as the basis for setting printing parameters through the Slic3r software, which sliced the stereolithography (STL) files of

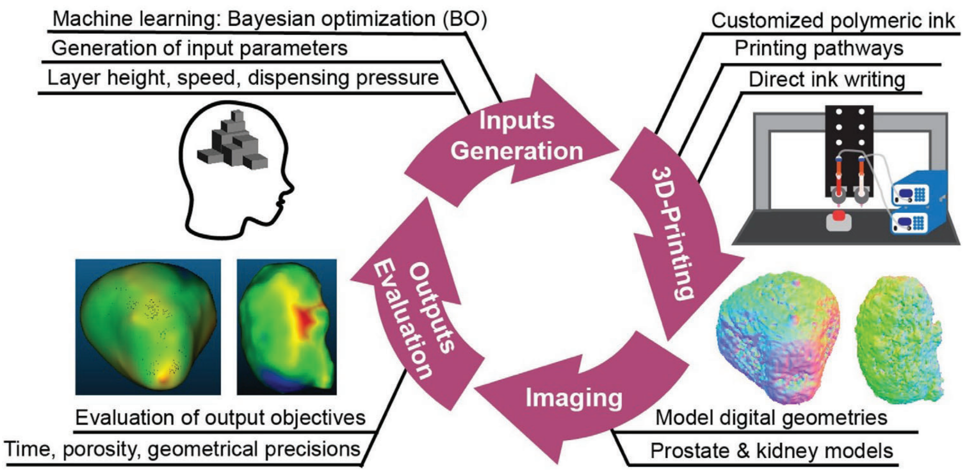

Figure 1. Flow-chart schematic of multi-objectiveBO assisted 3D-printing of presurgical organs models with three input parameters in tangent with four output parameters. The cycle starts with generating input values based on the current dataset of inputs and corresponding outputs through BO, which are used to produce printing pathways for direct-ink-writing (DIW). After the model is 3D-printed via DIW, image processing is applied to the model to reconstruct a mesh object. The mesh object is then adjusted for comparisons with the ideal model for measurements regarding positive and negative geometrical precisions. The time of model printing and porosity measurements are also calculated. Once all the output measurements are completed, their individual values are re-entered into the BO algorithm to yield new input parameters.

the organ models and generated G-code to guide our customized DIW 3D-printing system to fabricate the presurgical prostate and kidney models (Figure 2b; Movies S1 and S2, Supporting Information). The outputs were then evaluated during and after organ model printing. While printing occurred, we measured the entire printing duration to derive a time value for each model. After the four organ models (prostate or kidney) were printed using their initial four sets of inputs, image processing via Nvidia NeRF software was applied to reconstruct a mesh object (Movie S3, Supporting Information) for positive and negative precision values, which were calculated as an average distance between the mesh and ideal geometries of the organ models. Positive precision represents the amount of ink that is over-extruded, while negative precision represents the amount of ink that is under-extruded during printing. Subsequently, we defined and calculated the porosity as a mass difference between the printed model and ideal organ model. While the mass of printed model was directly measured, whereas the mass of the ideal organ model was calculated by the original STL model's volume times the ink density.

BO is a highly resource-efficient framework to solve global optimization problems using black-box evaluations of expensive objective functions. The key idea behind BO is to efficiently search for the optimal input parameters x that optimize $f(x)$, often referred to as the expensive black-box function. There are three key components of the BO framework which decide the parameters for the 3D printer in each iteration: 1) A surrogate model that captures our beliefs, based on past observations, about the printing parameters input-printed models output relationship; 2) An acquisition function that measures the utility of evaluating a candidate printer setting for optimizing the corresponding black-box objective function; and 3) An acquisition function optimizer that selects which printer setting with highest utility to evaluate next. In BO, Gaussian Processes (GPs)[52] are utilized as the underlying probabilistic surrogate models. GPs provide a flexible way to model the uncertainty associated with the objective function while being able to accurately estimate the objective function. GPs are a powerful tool in ML and optimization that can be used as surrogate models in various applications, including the 3D-printing optimization problem.

In many real-world problems, when domain practitioners are confronted with the challenge of balancing multiple, often conflicting objectives, the utilization of MOO is required. Unlike single-objective optimization tasks, which focus on optimizing a sole criterion, MOO becomes imperative when various aspects of the problem, such as accuracy, time, and precision, must be considered simultaneously. These diverse objectives often entail finding trade-offs. In the 3D-printing problem, altering different printing settings such as layer height, nozzle travel speed, and dispensing pressure could affect the precision, porosity, and printing duration of the printed shape in various ways. For example, improving shape precision requires sacrificing printing time and may lead to a higher porosity in the shape. Consequently, MOO techniques are deployed to discover a wide range of solutions, each representing a distinct trade-off among these objectives, rather than a single optimal solution. There are various algorithms proposed for solving the MOO problem. Some of the recent work on MOO using BO include Max-value Entropy Search,[53] Multi-Objective Regionalized BO,[54] Uncertainty-aware MOO,[55] and Expected Hypervolume Improvement (EH).[56]

We meticulously curated this input space, encompassing all conceivable combinations of these three decision variables, within the operational scope of the printer. The 4 objectives that we aim to optimize are printing time, shape porosity, negative precision, and positive precision. The GP for each objective function is defined using a Matern kernel with a prior of $\gamma(3.0, 6.0)$ for the length scale and a prior of $\gamma(2.0, 0.15)$ for the output scale. Each experiment is initialized with 4 randomly selected initial points. The reference point for each

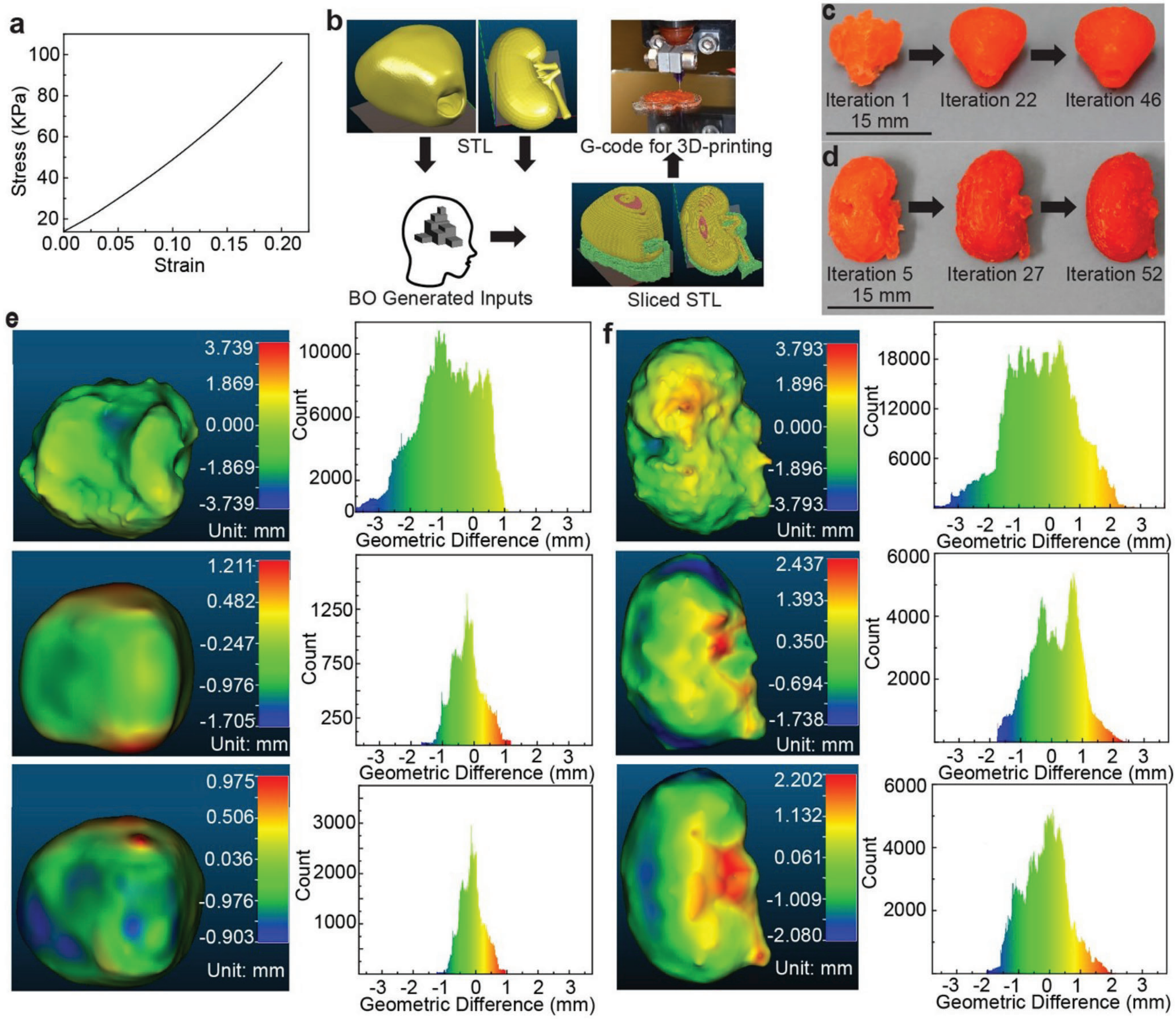

Figure 2. Machine-learning enabled design and optimization for 3D-printing of presurgical organ models and geometric fidelity analysis. a) Stress-strain correlation of the customized polymeric ink during mechanical compression test. b) 3D-printing the prostate and kidney models using a customized polymeric ink and BO generated inputs as the printing parameters. c) Photograph of the 3D-printed prostate models from iterations 1, 22, and 46 in chronological order to show growth in fidelity. d) Photograph of the 3D-printed kidney models from iterations 5, 27, and 52 in chronological order to show growth in fidelity. e,f) Calibrated distance maps and histograms of the organ model's external surfaces via 3D registration for geometric fidelity, between the respective 3D-printed prostate and kidney models (seen in c and d) with the corresponding ideal models based on original STL files.

experiment is defined as the lower bound of each of the objective functions.

The Pareto front is a set of non-dominated solutions, where no solution is universally better than another; instead, each solution represents a unique trade-off among the conflicting objectives. The mathematical definition clarifies that Pareto optimality involves both non-inferiority (no solution is worse in all objectives) and strict improvement (at least one objective is better). The Pareto front selected by the algorithm includes printed shapes that can be utilized in professional settings as they have negligible errors compared to the real model. The hypervolume indicator is a measure of how much of the objective space is dominated by the Pareto front. A larger hypervolume indicates a better set of solutions.

To verify the results of BO for 3D-printing, the initial 4 sets of inputs and the corresponding 4 sets of outputs from the evaluations of the initial 4 printed models were imported into the BO algorithm, to generate the first set of iteration inputs for repeating the four-step recursive process (iteration 1). The process was repeated for over 60 iterations of inputs and outputs for the prostate (Figure 2c) and kidney (Figure 2d) models, and it clearly indicates that with the increase of iteration numbers, the geometries of organ models became smoother and more accurate (Figure 2c,d). For the corresponding quantitative geometry fidelity, the calibrated distance maps of the external surfaces of the prostate and kidney via 3D registration are represented in Figure 2e,f. The results indicate the geometric differences between the 3D-printed organ models and the ideal models were narrowed down significantly with the increase of iteration numbers. For the prostate model, the geometric differences were distributed through surface voxels: −3.7 mm to 1 mm with peak at -1 mm (iteration 1), −1.5 mm to 1 mm with peak ≈0.2 mm (iteration 22) and -1 mm to 1 mm with peak at 0 mm (iteration 46). For the kidney model, the geometric differences were distributed through surface voxels: −3.5 mm to 2.5 mm with peak at 0.5 mm (iteration 5), −1.8 mm to 2.3 mm with peak at 1 mm (iteration 27) and -2 mm to 1.9 mm with peak at 0 mm (iteration 52).

Generally, the generated inputs demonstrated improved values across all the designated output areas as iterations increased (Tables S1 and S2, Supporting Information). The prostate model's first iteration had recorded time, porosity, positive precision, and negative precision values of 67 mins, −1.776 g, 0.399 mm, −1.194 mm. It was observed that the positive precision value in the first iteration was decent (dimensions of prostate and kidney models are 22.22 (L) x 20.66 (W) x 17.74 (H) mm^3 and 29.85 (L) x 20.82 (W) x 12.37 (H) mm^3 respectively), however this iteration's remaining three output objectives were significantly insufficient for obtaining an optimized printed model. Upon reaching iteration 22, each output objective became more desirable of time: 50 mins, porosity: −0.487 g, positive precision: 0.374 mm, and negative precision: −0.462 mm. These improvements are attributed to adjustments made in input parameters of the layer height and nozzle travel speed, leading to substantial advancements in the reaming three output objectives. Finally, iteration 46 showcased considerable progress in all output objectives with time: 43 mins, porosity: −0.033 g, positive precision: 0.184 mm, and negative precision: −0.303 mm. Similar trends were seen among the kidney model's growth as well. The measurements at iteration 5 for the kidney were time: 90 mins, porosity: −0.578 g, positive precision: 0.779 mm, and negative precision: −1.034 mm. Evidently, all four output objectives are insufficient for obtaining an optimized printed model. However, iteration 52 showed that it completely dominated iteration 5 in every area with time: 38 mins, porosity: −0.05 g, positive precision: 0.523 mm, and negative precision: −0.658 mm. Thus, iteration 5 was not included in the kidney's final Pareto front. **Figure 3a** (prostate model) and Figure 3b (kidney model) show how hypervolume indicators increased with the corresponding increase of iteration numbers, demonstrating convergence regarding hypervolume, which signifies better solution sets.

It is apparent that the application of the BO algorithm in the prostate model had explored a large amount of objective space during the first few iterations from iteration 1 to 5, which allowed for a large hypervolume indicator per the corresponding iteration range (Figure 3a). As a result, subsequent exploration and optimization led to a smoother hypervolume graph that began to plateau since there was less space to optimize. On the other hand, when the BO algorithm was applied to the kidney model, the hypervolume indicators between iterations 1 and 25 received notable increases as the iterations progressed (Figure 3b). This led to a rougher hypervolume graph during the aforementioned iteration range as the BO algorithm sporadically optimized and explored the objective space. However, after iteration 25, it was observed that the hypervolume graph started to smoothen out and reached a plateau. Therefore, the hypervolume graphs for both organ models displayed a smooth line at the concluding iterations when the convergence was reached, and subsequent iterations would minimally impact the hypervolume as an optimized set of solutions was established.

Analysis of each organ model's final Pareto front provides valuable insights into the fundamental trade-offs involved in optimizing each output objective. The Pareto front describes a collection of optimal input solution sets. Within the Pareto front, each individual solution set holds Pareto dominance, signifying their superiority over the other input solutions situated outside the front. These Pareto dominant solution sets possess an advantage over the non-dominant input solutions in terms of one or more output objectives, while simultaneously maintaining a standstill in the remaining objectives. Moreover, it is important to note that specifically each Pareto front solution set holds an equal degree of dominance over each other, as they possess an equivalent number of advantages. Here, it was observed that the Pareto front for both the prostate and kidney models evolved (Figure 3c,d) through various printing iterations (selected iterations 10, 20, 30, 40, 50, and 60). This evolution was influenced by the Pareto dominance of each newly generated solution, which led to alterations in the size of the Pareto front at varying iteration. In the Pareto front for the prostate model, the number of solution sets within the Pareto front generally stayed above or equal to 7 between iterations 10 and 40 (Figure 3c). However, some of the solution sets throughout the Pareto front during this range were either newly added or removed, signaling that convergence had not been fully reached yet. Between iterations 40 and 50, many of the Pareto front's solution sets were removed due to the addition of new solution sets that were highly dominant, reducing the size of the Pareto front. It was observed that between iterations 50 to 60, the only change in the Pareto front was the removal of solution set 5, demonstrating an optimized set of solutions. For the kidney's Pareto front (Figure 3d), a different trend was observed. Between iterations 10 to 60, the number of solution sets within the Pareto front only increased, with the removal of a few solution sets from the starting iterations. This indicated that many of the previous and additional solution sets within the Pareto front were uniquely dominant in output objectives, which developed a diverse Pareto front. Nonetheless, between iterations 50 to 60, the Pareto front did not receive any changes and exhibited convergence to an optimized set of solution.

The prostate model's final Pareto front, denoting the Pareto front present at the concluding iteration, contains 5 input solution sets with differing advantages and disadvantages (Figure 3e and Table S1, Supporting Information). In the solution set of iteration 3, a slight advantage was observed in terms of printing time compared to the remaining solutions in the final Pareto front. However, this advantage was countered by inferior performance in other objective areas. On the other hand, the solution set of iteration 17 achieved the best positive precision measurement, however, suffered substantially in terms of its negative precision value due to under-extrusion. In contrast, each solution set at iterations 42, 46, and 56 (Figure 3e and Table S2, Supporting Information), exhibited robust values in all output areas, though these values were slightly dominated in one or two specific areas. For instance, when compared to solution sets of iterations 7 and 17,

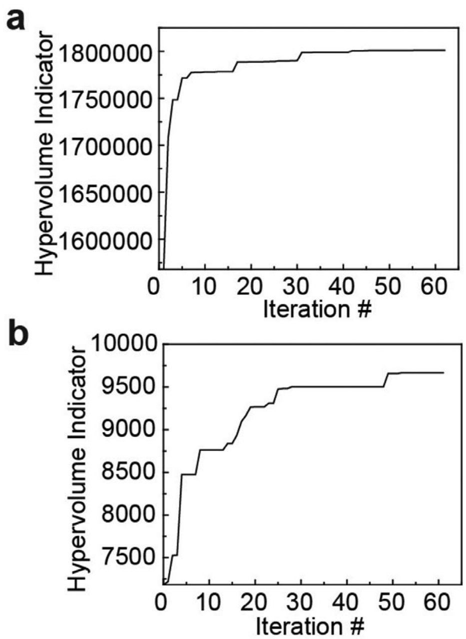

c

Iteration #	Solution sets in iteration # within the Pareto front
10	2, 3, 5, 6, 7, 8, 10
20	2, 3, 5, 6, 7, 8, 10, 14, 17, 20
30	3, 5, 7, 17, 23, 26, 29, 30
40	3, 5, 17, 26, 30, 31, 34, 35, 38
50	3, 5, 17, 42, 45, 46
60	3, 17, 42, 46, 56

d

Iteration #	Solution sets in iteration # within the Pareto front
10	2, 3, 4, 8
20	8, 16, 18, 19, 20
30	8, 16, 18, 19, 20, 23, 25, 26, 28
40	8, 16, 18, 19, 20, 23, 25, 26, 28
50	8, 16, 18, 19, 20, 23, 25, 26, 28, 46, 49, 52
60	8, 16, 18, 19, 20, 23, 25, 26, 28, 46, 49, 52

e

Inputs				Outputs			
Iteration #	Layer Height (mm)	Speed (mm/s)	Pressure (kPa)	Time (minutes)	Porosity (grams)	Precison(+) (mm)	Precison(-) (mm)
3	0.61	13.2	162.8	40	-0.557	0.374	-0.525
17	0.57	14.0	175.0	46	-0.423	0.144	-1.057
42	0.61	15.0	178.8	41	-0.006	0.266	-0.269
46	0.61	12.6	171.1	43	-0.033	0.184	-0.303
56	0.41	15.0	304.0	41	-0.023	0.191	-0.266

f

Iteration #	Layer Height (mm)	Speed (mm/s)	Pressure (kPa)	Time (minutes)	Porosity (grams)	Precison(+) (mm)	Precison(-) (mm)
8	0.61	11.9	169.7	40	-0.272	0.514	-0.711
16	0.61	15.0	179.0	38	-0.319	0.551	-0.593
25	0.41	15.0	345.0	61	0.008	0.620	-0.518
49	0.60	15.0	179.0	38	0.668	0.907	-0.446
52	0.61	15.0	178.9	38	-0.050	0.523	-0.658

Figure 3. Analysis of the progression and dominance of input solution sets over ≈60 iterations. a,b) Measurements of hypervolume, which refers to the quantity of objective space covered by input solutions, for the prostate model and kidney model, respectively. c,d) Table of input solution sets within the Pareto front at varying iterations for the prostate model and kidney model, respectively. e,f) Table of input solution sets within the final Pareto front and their individual values regarding the inputs and corresponding output values, for the prostate model and kidney model, respectively. (Iterations 42, 46, 56 (bold) in Figure 3e yielded the most optimal prostate models and iteration 52 (bold) in Figure 3f yielded the most optimal kidney model).

all three of the previously mentioned sets had marginally worse time and positive precision values, respectively.

Conversely, when comparing the final Pareto fronts of the kidney model and the prostate model, moderate differences were observed in terms of diversity and size (Figure 3f). The kidney model's Pareto front consisted of 12 distinct solution sets, whereas the prostate model's Pareto front was relatively smaller. This distinction arose from a lower degree of Pareto dominance, perceived across the entire spectrum of solutions. For instance, the solution set of iteration 8 came closest to achieving an optimal positive precision value and had a decent negative precision value but encompassed a subpar porosity. Noticeably, the solution set of iteration 52 appeared to display the most optimal time value while maintaining adequate measurements in all other aspects. Similarly, the solution set of iteration 49 also presented the best time value while holding a slight advantage over the solution set of iteration 52 regarding negative precision. However, the solution set of iteration 49 experienced drastic shortcomings in the remaining parameters. Another particular highlight is the solution set of iteration 25, which achieved a nearly perfect porosity value. Nevertheless, it is hindered by an extended time value and a slightly higher positive precision value.

It is essential to recognize that the optimized 3D printing settings can vary significantly depending on the specific object being printed. In this study, our objective was to determine the optimal configuration specifically for presurgical organ models. Unlike standard ML tasks, which aim to train a predictive model that generalizes to unseen inputs, the primary goal of BO is to identify the optimal solutions for a predefined set of target objectives. The training process in BO was designed to facilitate the identification of these optimal configurations. The primary focus of our study was not to conduct an exhaustive validation across a wide range of scenarios and materials, but rather to establish the effectiveness of our optimization algorithm within a controlled experimental setting which allowed us to showcase the practical application of our method.

Additionally, our multi-objective BO algorithm was designed to be broadly generalizable, capable of adapting to various materials and achieving robust results across other disciplines without extensive modifications to the core algorithm. In practice, adjusting the specific output parameters and input space is necessary due to material-specific and object design requirements. These requirements often arise from different materials and designs interacting with the 3D printer in unique ways, requiring a distinct set of printer settings to achieve an optimal result. For example, we used customized ink with an 8:4.5 weight ratio of silicone sealant to silicone grease as our printing material. Three possible scenarios based on material or design requirements are described as follows: 1) Suppose we wanted to print a mimicked brain tissue model using an ink with lower mechanical properties; it would become imperative for us to increase the amount of silicone grease in the ink. Consequently, since silicone grease is significantly less viscous than silicone sealant, our input space would drastically change as it represents the set of all reasonable 3D-printing configurations. The ink's lower viscosity would allow for a decreased dispensing pressure range, both at the lower and upper bounds, since less viscous ink flow out quickly. 2) Meanwhile, if our goal was to print a thin tissue such as gastric mucosa (stomach lining), which typically measures between 1 to 1.5 mm in thickness, a set of smaller nozzle diameters for our input space would be more suitable. For example, utilizing our current input space, consisting of larger nozzle diameters ranging from 0.33 to 0.61 mm, would result in inferior printing results since it would be difficult to print such a thin design accurately. Therefore, it would be impossible to find an optimal set of 3D-printing configurations within the search space. Instead, it would be appropriate to use a nozzle diameter range between 0.1 and 0.2 mm. 3) In the case of printing the tongue, it would be valuable to include texture as one of the output parameters. Texture can be characterized as the average surface roughness by using an optical profilometer. The measured values would be numerical, similar to the current output objectives. Specifically, they represent the mean of the absolute values of the surface height deviations calculated from the reference line over a given length. The reference line goes through the mean height of the surface's bumps and valleys. Thus, we would be able to optimize for the tongue's tiny bumps (papillae) located at its surface.

Hence, we have shown that our multi-objective BO has proven highly effective in optimizing expensive-to-evaluate objective functions regarding optimizing 3D-printing configurations, surpassing traditional methods. Existing optimization techniques in the field often require substantial computational and physical lab resources and frequently underperform when compared to our proposed multi-objective BO approach. The EHVI algorithm we utilized is not only computationally efficient but also straightforward to implement, making it an excellent choice for interdisciplinary applications. Given the constraints on both time and financial resources, we prioritized our budget to conduct experiments on additional presurgical organ models rather than benchmarking against other baselines. This decision allowed us to better demonstrate the versatility and practical applicability of our method. By focusing on these experiments, we provided a compelling validation of our algorithm's performance in real-world scenarios.

Practitioners looking into implementing our techniques in real-world scenarios will benefit from considering ways to automate our steps, thus achieving even greater time and labor efficiency. For example, the primary hardware component used in our image processing was a camera. This step could be automated with a device that either spins the desired 3D-printed object or camera in 360 degrees and uploads the recorded data to our software. Nonetheless, complete automation necessitates custom-built hardware, providing a potential challenge. In general, practitioners face challenges regarding time and financial costs due to resources and the nature of optimization problems. However, these challenges widely depend on the practitioner's intent. In our study, the ink used did not pose a financial difficulty.

3. Conclusions

In summary, we developed a four-step, principled methodology for generating the optimal solution set that aims to define key input parameters, which can be applied to DIW 3D-printing for presurgical organ models and other functional devices. Our use of BO allows us to efficiently search through the large input space and visualize the trade-offs between each solution set with the Pareto front. Our final Pareto front for the prostate model provides a set of three input solutions that are exceptionally optimal. Although the kidney model seemed to perform slightly worse regarding precision, the reason is due to the kidney's small details regarding its vessels. However, it is essential to highlight that had we employed larger models for both the prostate and kidney, the precision values would likely have shown superior performance relative to their sizes. This correlation is due to precision being primarily influenced by external geometry. Nevertheless, our capability to consistently generate optimal models with high-fidelity, provides a proof of concept that can be applied to other disciplines. The outcome of this work paves the way for optimizing input and output parameters that pertain to manufacturing functional devices and structures for a variety of desired properties, such as drag force, texture, and mechanical properties. Thus, we can further refine the accuracy and utility of our models, making them valuable tools for a wide range of applications beyond what we have explored in this study.

4. Experimental Section

Customized Polymeric and Supporting Ink Formulation for 3D-Printing: The printing ink compound was formulated with a bulking agent: silicone grease (#LP20, Trident), active agent: silicone sealant (Loctite SI 595 CL with acetoxy-curing and room temperature vulcanization), and coloring solution: red coloring agent (Procyinyl Red GS, ICI America Inc.) combined with dichloromethane (DCM) solvent. The weight ratio of the bulking agent to active agent for the ink was 4.5:8 (w/w). The coloring solution contained 0.5 mL of DCM and 1% (w/v) coloring agent with a 25:1 (w/v) ratio to the total silicone component (12.5 g). All three substances were mixed via a centrifugal mixer (ARE-310, Thinky) at 2,000 rpm for 8 min. The supporting ink consisted of Pluronic 127 (Sigma–Aldrich) diffused in a glycerol/deionized water solution (1:9 v/v) with a 2:5 (w/v) ratio and provided temporary structural assistance for overhanging and complex model features.[4]

Mechanical Properties of the Customized Ink: It was printed multiple cylinders using the specified ink, each with a diameter and height of 10 mm. To evaluate their mechanical properties, these cylinders to a static compression test using specialized mechanical testing equipment (Instron 600DX) was subjected. During the test, a load cell with a capacity of 50 lbs was utilized and traveled a distance of 9.5 mm downwards (within the travel limit of the machine) at a controlled rate of 0.5 mm $^{-1}$s. The focus for data collection was on the initial deformation behavior occurring at the strain range between 0.00 and 0.20, which corresponds to a stress range of 0 to 100 kPa. By carefully analyzing the linear correlation between stress and strain within this specified range, the Young's modulus of 407.5 Pa was determined for the customized ink material.

BO Surrogate Model: The acquisition function uses the surrogate model of the figure-printer setting relationship $\hat{f}(x)$ to decide which printer setting to evaluate next while striking a balance between exploitation and exploration. The BO surrogate model was a probabilistic model of the shape-printer setting relationship $f(x)$ trained on all available observations $\{(x_i,\ y_i = f(x_i))\}_{i=1,\ldots,n}$ from past experiments. Typically, the surrogate model treats $f(x)$ as a random variable that follows a Gaussian distribution $f(x) \sim N(\hat{y}(x), \sigma^2(x))$ With mean $\hat{y} \in \mathbb{R}$ and variance $\sigma^2 \in \mathbb{R}$. The surrogate model reflects the current beliefs about $f(x)$ and serves two purposes in BO. First, in order to guide exploitation, $\hat{y}(x)$ cheaply estimates the properties of the remaining, unevaluated printer settings as $\hat{y}(x)$ is a cheap-to-evaluate approximation of the expensive objective function $f(x)$. Second, in order to guide exploration, $\sigma^2(x)$ quantifies the uncertainties in the predicted printed figure properties of the unevaluated printer settings. This uncertainty estimate makes us aware of "blind spots" of the surrogate model; These spots were regions in the printer setting space that it was need to explore to improve the approximation of $\hat{y}(x)$ and reduce the uncertainty in this beliefs about $f(x)$. The surrogate model was updated every time new data points in the form of input-output pairs $(x_{n+1},\ y_{n+1} = f(x_{n+1}))$ were observed. This update process was crucial as it continually refines the model's understanding of the objective function as the mean function $\hat{y}(x)$ is updated to incorporate the newly observed data, and the variance $\sigma^2(x)$ is adjusted accordingly. This process ensures that the GP model adapts to the known data and improves its approximation of the expensive objective function after every iteration while still capturing the uncertainty in unexplored regions of the input space.

BO Acquisition Function: To determine where to sample the objective function, BO employs an acquisition function. The acquisition function $AF(x;\ f\ (x))\ :\ X\ \rightarrow\ \mathbb{R}$ scores the utility of, next, evaluating printer setting $x \in X$ with the expensive objective function f. Here, "utility" was defined in terms of the ultimate goal of finding the optimal set of printer settings for printing the selected model defined as x^*, with the fewest experiments. The acquisition function employs the prediction of the property $\hat{y}(x)$ and the associated uncertainty σ^2 from the surrogate model $\hat{f}(x)$ to assign a utility score to the printer setting that balances exploitation and exploration, respectively. Maxima of the acquisition function were located in regions of printer setting space where the predicted property was large, or the uncertainty is high. Some of the commonly used acquisition functions in BO were the Expected Improvement (EI),[57] Upper Confidence Bound (UCB),[58] and Thompson Sampling (TS).[59] The EI acquisition function measures the expected improvement in the objective function value over the current best-known optimal point f_{opt}, at a given point x.

BO Acquisition Function Optimization: The decision of which printer setting to evaluate next is made by maximizing the acquisition function: $x_{n+1} = argmax_{x \in X \setminus X_n} AF(x, f_n^{\wedge}(x))\ x_{n+1}$ where $X_n = \{x_1, \ldots, x_n\}$ is the set of n printer settings that have been evaluated already. Importantly, the acquisition function must be cheap to evaluate and optimize. BO proceeds iteratively through these key steps. First, the GP model was updated with observed data. Then, the acquisition function was optimized to select the next sampling point that maximizes it. Subsequently, the expensive objective function was evaluated at the chosen point, and the new data point was added to the observed data. This iterative loop continued until a predefined stopping criterion, such as a maximum number of iterations or convergence threshold, was met.

Multi-Objective Optimization: Without loss of generality, MOO was defined as the problem of maximizing $K \geq 2$ real-valued objective functions $\{f_1(x), \ldots, f_K(x)\}$ over the given printer setting parameter space $X \subseteq \mathbb{R}^d$ where d is the number of decision variables and each decision variable's boundaries were pre-defined by an expert domain practitioner with respect to its corresponding feasible printer setting. A printing experiment with candidate printer setting parameters $x \in X$ generated a vector consisting of objective values $y = \left(y_{f_1}, \ldots, y_{f_K}\right)$ where $y_{f_j} = f_j(x)$ for all $j \in \{1, \ldots, K\}$. The goal of this MOO problem was to find a set of decision variables X^* that maximize the vector of objective functions $f(x^*)$ while respecting the boundaries of the decision variables without Pareto-dominating each other. The input vector x Pareto-dominates another input vector x′ if $f_j(x') \leq f_j(x)\ \forall j$ and there exists some $j \in \{1, \cdots,\}$ such that $f_j(x') < f_j(x)$. The optimal solution of the MOO problem is a set of input vectors $X^* \subset X$ such that no configuration $x' \in X \setminus X^*$ Pareto-dominates another. The solution set X^* is called the optimal Pareto set and the corresponding set of function values Y^* is called the optimal Pareto front. The most commonly used measure to evaluate the quality of a given Pareto set is by calculating the Pareto hypervolume (PHV) indicator[60] of the corresponding Pareto front of $\left(y_{f_1}, \ldots, y_{f_K}\right)$ with respect to a reference point r. The overall goal was to approximate the Pareto set X^* by minimizing the total number of expensive function evaluations. The Pareto Front (PF) was defined as $PF = \{x \in X \mid \nexists\, x' \in X,\ x' \neq x,\ \text{ such that } \forall k,\ f_k(x') \leq f_k(x) \text{ and } \exists m\ f_m(x') < f_m(x)\}$. A solution x belongs to the Pareto front if there was no other feasible solution x' in the decision space X that can simultaneously improve or equal all M objectives compared to x and strictly improve at least one objective.

3D-Printing Problem Setup: Suppose a 3D printer with a large number of different combinations was had, how it could adjust its settings for printing an organ. Let f: $X \rightarrow R$ be a black-box objective function that, given a specific setting on the printer $x \in X$, returns a relevant property of the printed shape $y = f(x)$. Each evaluation of f corresponds to performing an expensive experiment -in terms of time and the value of the printing material- to measure the printing time, precision, and porosity y of printer setting x. This goal was to find the highest-performing set of setting X^* from X that maximize the PHV indicator while conducting the fewest number of expensive experiments. It could interpret $f(x)$ as the unknown printer setting-shape relationship since x represents a unique setting on the printer, and evaluating f means conducting an experiment to measure its property, y. Suppose a 3D printer with a large number of different combinations was had, how it could adjust its settings for printing an organ. Let f: $X \rightarrow R$ be a black-box objective function that, given a specific setting on the printer $x \in X$, returns a relevant property of the printed shape $y = f(x)$. Each evaluation of f corresponds to performing an expensive experiment -in terms of time and the value of the printing material- to measure the printing time, precision, and porosity y of printer setting x. This goal was to find the highest-performing set of setting X^* from X that maximize the PHV indicator while conducting the fewest number of expensive experiments. It could interpret $f(x)$ as the unknown printer setting-shape relationship since x represents a unique setting on the printer, and evaluating f means conducting an experiment to measure its property, y. GPs were a powerful tool in ML and optimization that can be used as surrogate models in various applications, including the 3D-printing optimization problem. GPs serve as a versatile framework for characterizing stochastic processes with joint Gaussian distributions across any number of input locations. Essentially, GPs provide probability distributions over functions, enabling the generation of function samples from them. In the case of this 3D-printing MOO problem, GPs play a pivotal role by modeling the objective function as a sample drawn from the GP. The non-parametric nature, adaptability, and resilience of GPs make them well-suited for hyperparameter estimation, avoiding overfitting even with limited data. In the absence of any observed data, GPs can serve as a prior, allowing the generation of smooth functions without the need for prior observations. According to the GP prior, a function's potential values at any given input location are characterized by a mean (typically zero) and a standard deviation. GPs to predict the behavior of black-box functions based on a small number of observations was used. Given a set of printer settings, and the corresponding printed shape's output values, a GP to predict the output value for a new unobserved printer setting was used. Gaussian Processes $GP_1, \cdots, GP_4$ for the four objective functions corresponding to time, shape precision, and shape porosity from the training data in the form of past printed figures was built. These statistical models can predict the output of unknown printer settings and also quantify their uncertainty for those predictions. In each iteration of this algorithm, the learned statistical models were employed to select the next candidate printer settings for evaluation via printing a new figure.

Expected Hypervolume Improvement Acquisition Function: To formally define, Given a reference point, $r \in R^K$ the hypervolume indicator of a finite approximate Pareto set P is the M-dimensional Lebesgue measure λ_K of the space dominated by P and bounded from below by $r : HV\ (P,\ r) = \lambda_K\ (\cup_{\mathrm{i}=1}^{|\mathrm{P}|}[\mathrm{r}, \mathrm{y_i}])$ where $[r, y_i]$ denotes the hyper-rectangle bounded by vertices r and y_i. Considering the definition of the hypervolume the hypervolume improvement (HVI) was defined. Given a Pareto set P and reference point r, the HVI of a set of points Y is $HVI\ (Y, P, r) = HV(P \cup Y, r) - HV(P, r)$. EHVI was defined as the expectation of HVI over the posterior distribution $P(f,\ D)$ over the true function values f given the observed data DError! Bookmark not defined. Mathematically, it is defined as $\alpha_{EHVI}(X_{candidates}) = E[HVI(f(X_{candidates}))]$. EHVI was a way to measure the potential benefit of adding a new candidate solution to the existing set of non-dominated solutions in MOO. It quantifies how much the hypervolume of the Pareto front was expected to improve when the new solution was added, helping the optimization algorithm focus on areas of the objective space that were not well-covered by the current solutions. In order to solve the aforementioned problem, a multi-objective BO method using GPs as surrogate models and the EHVI acquisition function was proposed. The algorithm requires a meticulous formulation of the MOO problem that was germane to the ML application. To prevent the selection of infeasible printer settings during the BO exploration, it was first established a feasible input space for printer settings defined by expert domain practitioners. The BO method will then select optimal points from within this defined space. Following the formulation of the optimization problem, the method proceeds with the selection of an initial set of printer settings. This set of initial samples are generated by random selection. These initial samples serve as the foundational dataset upon which the initial GP models are constructed for each expensive black-box objective function. As the surrogate models, was used Gaussian Processes. To aptly encapsulate the intricate nature of the objective functions, the Matérn 5/2 kernel, renowned for its adaptability, was utilized as the GP kernel. The GPs were trained using the initial points and the objective values calculated from the printed shape. All values were min-max normalized at the beginning of the algorithm and after each iteration to decision variable boundaries pre-defined by domain experts. The optimization process proceeds iteratively, with an initial empty set symbolizing the Pareto front. Consequently, this Pareto front was updated as the optimization process unfolds. Guided by the EHVI acquisition function, candidate solutions were systematically selected. The EHVI function strikes a balance between exploration, which encourages the exploration of uncertain regions, and exploitation, which evaluates potential improvements in the objective space. The EHVI acquisition function was calculated on all points in the input space, and then it was optimized to select the next candidate point. The selected candidate solution was then assimilated into the evolving Pareto front. Subsequently, the GP models were updated with the newly acquired data point, thus refining the probabilistic predictions for the objective functions. This iterative process persists until it was saw convergence in the results. A pseudocode of the method was included in (Supporting Information Algorithm S1).

Determining the Input Parameters and Space: The input parameters include layer height, nozzle travel speed, and dispensing pressure (supporting ink excluded) which greatly influences the printed model's output in multiple areas such as geometry. The input space for each tested model through printing cylinders of 10 mm diameter and 10 mm height with varying input parameters per nozzle with inner diameters of 0.33 mm, 0.41 mm, 0.51 mm, and 0.61 mm (including the following categories) was determined. Each nozzle had a unique layer height range (mm) and dispensing pressure (kPa) range in response to the selected speed of [0.26, 0.33] and [285.0, 470.0], [0.34, 0.41] and [211.0, 345.0], [0.42, 0.51] and [125.0, 250.0], and [0.52, 0.61] and [98.0, 179.0], respectively. The nozzle travel speed range of 4.0 mm $^{-1}$s to 15.0 mm $^{-1}$s was consistent among all nozzles. The input space was suitable for all types of models using the specified ink.

Determining the Output Parameters and Space: The output parameters include time, porosity, positive precision, and negative precision which provide valuable metrics in determining the model's efficiency and fidelity. Time represents the length of the 3D-printing process and was measured from when the printhead first traveled to when it fully stopped. Porosity refers to the voids within the printed model that affect its mechanical properties and was measured through calculating the mass difference between the print and ideal model. The ideal weight for each model to be 3.767 g through multiplying the STL volume (≈3711 mm^3) by the density of silicone sealant (1.015 g mm^3) (Loctite SI 595 CL) was calculated. Although the density of silicone grease (≈1.0 g mm^3) (#LP20, Trident) slightly varies from silicone sealant, it minimally affects calculations. Positive and negative precision determines the overall geometric fidelity of the print and the amount of over/under extrusion. Precision (mm) was measured as an average distance between the surface of the printed and ideal model through image processing via Nvidia's NeRF A.I. and 3D registration via CloudCompare. The output space was determined through testing individual edge cases for each parameter regarding the lower and upper bounds. Since the BO algorithm was designed for maximization, where larger values were more desirable, each output value was made negative (partial negative data in time, porosity and positive precision have been adjusted in the Tables S1 and S2, Supporting Information for better understanding). The prostate model's boundaries for the output space were time: −360 to −10 min, porosity: −20 to 0 g, positive and negative precision: −20.0 to 0 mm. These boundaries were heavily expanded to account for outliers resulting in a longer BO computational time. For the second experiment using the kidney model, we implemented a tighter range for each parameter being time: −230 to −37 min, porosity: −4 to 0 grams, positive and negative precision: −4 to 0 millimeters, which allowed the BO calculations to run significantly quicker.

Organ Model 3D-Printing: The human prostate STL model was patient-specific and developed via Vitrea software with MRI image data.[3] Conversely, the kidney STL model was obtained from RenderHub, and provided a general anatomical representation of a human kidney's surface features with partial inclusion of the renal vein/artery and ureter for added geometric complexity. Each model was scaled down to 50% of the prostate model's volume (prostate: 22.22 (L) x 20.66 (W) x 17.74 (H) mm^3, kidney: 29.85 (L) x 20.82 (W) x 12.37 (H) mm^3) to increase printing efficiency. The STL models were sliced into horizontal layers (Figure 2b) via Slic3r, an open-source software, to produce a 3D-printing programing language (G-code) which determined the printing pathways. The G-code was entered into a customized 3D-printing system (AGS1000, Aerotech), fitted with two independent z-axis heads, which held two ink syringe barrels (Optimum, Nordson EFD) individually containing the supporting and polymeric ink. The rate of deposition was dictated by two high-accuracy dispensers (Ultimus V, Nordson EFD). Precision nozzles (Nordson EFD) with inner diameters of 0.33 mm (23 GA GP.013X.25), 0.41 mm (22 GA GP.016X.25), 0.51 mm (21 GA GP.020X.25), and 0.61 (20 GA GP.023X.25) were used to print layers with heights ranging from 0.26 mm to 0.61 mm respectively. After the printed model has been fully cured in room temperature, the supporting ink was separated from the model via water flushing at 4 °C.

Image Processing for Organ Models: In order to capture the geometry of the 3D-printed organs to develop a model for comparisons, an image processing approach was used. First, a 360° video recording was taken of the printed model and reconstructed with Nvidia's open-source, A.I. neural radiance field (NeRF) to generate a mesh object that is composed of polygons and vertices.[61] Within the NeRF program, the model would be isolated from its surroundings with the crop box feature. The exported mesh was then smoothened and re-meshed for full solidification with Blender, an open-source software. However, distinct features caused by under/over extrusion remained present. The final prostate and kidney mesh generally contained between 50 000–600 000 faces and vertices, with 100 000–1 200 000 triangles. The substantial range was because each model contained unique complex features from varying input parameters. Although the ideal prostate STL has a singular, hollow urethra channel, capturing the internal geometry was unfeasible as the NeRF program could only capture the surficial concavity of the channel opening. Therefore, the ideal prostate model's inner channels were filled via Blender and accurate concavity was demonstrated. The ideal prostate model was exported as a mesh object which contained 477186 vertices and faces with 954368 triangles. The kidney STL does not have this limitation, and the original mesh object was used for printing and comparisons. The kidney mesh contained 3656 vertices with 7296 vertices and triangles.

3D Registration for Geometric Precision: To measure the positive and negative precision values, a 3D registration procedure was executed to develop a histogram and a map of calibrated distances (mm) between points on the exterior of the printed model's scaled mesh object and ideal organ mesh object, for surface comparisons. CloudCompare, an open-source software, was utilized for this procedure. For the prostate and kidney model, a total of 50 000–200 000 and 500 000–1 000 000 surface points were compared respectively. For each point on the printed organ model, a comparison was made with its nearest counterpart on the ideal model, measuring the distance between them. The resulting histogram of calibrated distances was divided into two separate histograms: one containing only positive values and the other containing purely negative values. The average distance value of each individual histogram was used for positive and negative precision respectively. To align with the maximization objective of the BO algorithm, the negative absolute value was applied to the precision values. For the prostate model, the greatest positive and negative precision value achieved was −0.144 and −0.266 mm respectively.

Supporting Information

Supporting Information is available from the Wiley Online Library or from the author.

Acknowledgements

E.S.C. and A.A. contributed equally to this work. Prof. K.Q. acknowledges WSU Startup Funds and Cougar Cage Funds, and National Science Foundation (Research Traineeship program, Award No. DGE 2244082). Prof. J.R.D. acknowledges National Science Foundation (Award No. IIS-1845922). The authors acknowledge Data Depository for University of Minnesota (https://doi.org/10.13020/rbvt-5s33) for downloading original STL file for a prostate model, and the model file was also originally used in Prof. K.Q. prior research work. The authors thank Robert Lentz in Mechanics of Materials Laboratory in Engineering Teaching Research Laboratory (ETRL) Building at WSU for mechanical test support. The authors also thank C.C. from WSU School of Mechanical and Materials Engineering, for their valuable early contributions for this work.

Conflict of Interest

The authors declare no conflict of interest.

Data Availability Statement

The data that support the findings of this study are available from the corresponding author upon reasonable request.

Keywords

3D-printing, Bayesian optimization, machine learning, parameters optimization, presurgical organ models

Received: January 9, 2024
Revised: June 29, 2024
Published online:

[1] I. S. Yoon, Y. Oh, S. H. Kim, J. Choi, Y. Hwang, C. H. Park, B.-K. Ju, *Adv. Mater. Technol.* **2019**, *4*, 1900363.
[2] J. Goole, K. Amighi, *Int. J. Pharm.* **2016**, *499*, 376.
[3] K. Qiu, Z. Zhao, G. Haghiashtiani, S.-Z. Guo, M. He, R. Su, Z. Zhu, D. B. Bhuiyan, P. Murugan, F. Meng, S. H. Park, C.-C. Chu, B. M. Ogle, D. A. Saltzman, B. R. Konety, R. M. Sweet, M. C. McAlpine, *Adv. Mater. Technol.* **2018**, *3*, 1700235.
[4] G. Haghiashtiani, K. Qiu, J. D. Z. Sanchez, Z. J. Fuenning, P. Nair, S. E. Ahlberg, M. C. Mcalpine, *Sci. Adv.* **2020**, *6*, eabb4641.
[5] S. Z. Guo, K. Qiu, F. Meng, S. H. Park, M. C. McAlpine, *Adv. Mater.* **2017**, *29*, 1701218.
[6] Q. Yi, S. Najafikhoshnoo, P. Das, S. Noh, E. Hoang, T. Kim, R. Esfandyarpour, *Adv. Mater. Technol.* **2022**, *7*, 2101034.
[7] S. H. Park, R. Su, J. Jeong, S.-Z. Guo, K. Qiu, D. Joung, F. Meng, M. C. McAlpine, *Adv. Mater.* **2018**, *30*, 1803980.
[8] M. E. Kupfer, W.-H. Lin, V. Ravikumar, K. Qiu, L. Wang, L. Gao, D. B. Bhuiyan, M. Lenz, J. Ai, R. R. Mahutga, D. Townsend, J. Zhang, M. C. McAlpine, E. G. Tolkacheva, B. M. Ogle, *Circ Res.* **2020**, *127*, 207.
[9] S. Adepu, N. Dhiman, A. Laha, C. S. Sharma, S. Ramakrishna, M. Khandelwal, *Curr. Opin. Biomed. Eng.* **2017**, *2*, 22.
[10] J. Lipskas, K. Deep, W. Yao, *Sci. Rep.* **2019**, *9*, 3746.
[11] Y. Pang, Y. Cao, Y. Chu, M. Liu, K. Snyder, D. MacKenzie, C. Cao, *Adv. Funct. Mater.* **2020**, *30*, 1906244.
[12] Z. Lyu, G. J. H. Lim, J. J. Koh, Y. Li, Y. Ma, J. Ding, J. Wang, Z. Hu, J. Wang, W. Chen, Y. Chen, *Joule* **2021**, *5*, 89.
[13] Z. Wang, W. Li, L. Chen, Z. Zhan, H. Duan, *ACS Appl. Poly. Mater.* **2022**, *4*, 2384.
[14] S. Zhang, Y. Liu, J. Hao, G. G. Wallace, S. Beirne, J. Chen, *Adv. Funct. Mater.* **2022**, *32*, 2103092.
[15] S. Henn, C. Carpien, *3-D Printer Brings Dexterity to Children with No Fingers, National Public Radio, June 18*, **2013**.
[16] R. Thorsen, D. Cugnod, M. Ramella, R. M. Converti, M. Ferrarin, *Assist. Technol.* **2024**, *36*, 16.
[17] M. Khorasani, A. H. Ghasemi, B. Rolfe, I. Gibson, *Rapid Prototyp. J.* **2022**, *28*, 87.
[18] V. Madhavadas, D. Srivastava, U. Chadha, S. Aravind Raj, M. T. H. Sultan, F. S. Shahar, A. U. M. Shah, *CIRP Ann. Manuf. Technol.* **2022**, *39*, 18.
[19] M. A. S. R. Saadi, A. Maguire, N. T. Pottackal, M. S. H. Thakur, M. M. Ikram, A. J. Hart, P. M. Ajayan, M. M. Rahman, *Adv. Mater.* **2022**, *34*, 2108855.
[20] T. Uchida, H. Onoe, *Micromachines* **2019**, *10*, 433.
[21] X. Wan, L. Luo, Y. Liu, J. Leng, *Adv. Sci.* **2020**, *7*, 2001000.
[22] A. Shahzad, I. Lazoglu, *Composites, Part B* **2021**, *225*, 109249.
[23] J. Maurath, N. Willenbacher, *J. Eur. Ceram. Soc.* **2017**, *37*, 4833.
[24] A. Mantelli, A. Romani, R. Suriano, M. Levi, S. Turri, *Adv. Engineer. Mater.* **2021**, *23*, 2100116.
[25] X. Peng, *Addit. Manuf.* **2021**, *40*, 101911.

[26] S. F. Iftekar, A. Aabid, A. Amir, M. Baig, *Polymers* **2023**, *15*, 2519.
[27] F. Yang, *LWT* **2018**, *87*, 67.
[28] T. S. Tamir, G. Xiong, Q. Fang, Y. Yang, Z. Shen, M. Zhou, J. Jiang, *Int. J. Comp. Integrat. Manuf.* **2023**, *36*, 1362.
[29] G. D. Goh, S. L. Sing, W. Y. Yeong, *Artif. Intellig. Rev.* **2021**, *54*, 63.
[30] T. Erps, M. Foshey, M. K. Lukovic, W. Shou, H. H. Goetzke, H. Dietsch, K. Stoll, B. von Vacano, W. Matusik, *Sci. Adv.* **2021**, *7*, eabf7435.
[31] B. Singh, R. Kumar, J. S. Chohan, *Mater. Today: Proceed.* **2022**, *48*, 981.
[32] X. Wang, J. Cao, Y. Cao, *Rapid Prototyping J.* **2023**, *29*, 246.
[33] L. F. Cruz, F. B. Pinto, L. Camilotti, A. M. O. Santanna, R. Z. Freire, L. dos Santos Coelho, *Annals Operat. Resear.* **2022**, *319*, 1565.
[34] S. Freeman, S. Calabro, R. Williams, S. Jin, K. Ye, *Front. Bioengineer. Biotechnol.* **2022**, *10*, 913579.
[35] H. Chen, Y. Liu, S. Balabani, R. Hirayama, J. Huang, *Research* **2023**, *6*, 0197.
[36] M. F. Khan, *Mater. Today: Proceed.* **2021**, *42*, 521.
[37] D. A. Brion, S. W. Pattinson, *Nat. Commun.* **2022**, *13*, 4654.
[38] V. Kadam, S. Kumar, A. Bongale, S. Wazarkar, P. Kamat, S. Patil, *Appl. Sys. Innov.* **2021**, *4*, 34.
[39] M. Ackermann, C. Haase, *Addit. Manuf.* **2023**, *71*, 103585.
[40] P. Akbari, F. Ogoke, N. Y. Kao, K. Meidani, C. Y. Yeh, W. Lee, A. B. Farimani, *Addit. Manuf.* **2022**, *55*, 102817.
[41] M. Piovarci, Closed-loop control of direct ink writing via reinforcement learning. *arXiv preprint arXiv:2201.11819*, **2022**.
[42] B. Shahriari, K. Swersky, Z. Wang, R. P. Adams, N. de Freitas, *Proceedings of the IEEE* **2015**, *104*, 148.
[43] J. Snoek, H. Larochelle, R. P. Adams, *Adv. Neural Informat. Process. Sys.* **2012**, *25*.
[44] W. Lyu, et al., *IEEE Transactions on Circuits and Systems I: Regular Papers* **2018**, *65*, 1954.
[45] Z. Zhou, in *2020 Design, Automation & Test in Europe Conference & Exhibition (DATE)*. **2020**.
[46] R. Priem, N. Bartoli, Y. Diouane, A. Sgueglia, *Aerospace Sci. Technol.* **2020**, *105*, 105980.
[47] A. Deshwal, C. M. Simon, J. R. Doppa, *Mol. Syst. Des. Eng.* **2021**, *6*, 1066.
[48] Q. Liang, A. E. Gongora, Z. Ren, A. Tiihonen, Z. Liu, S. Sun, J. R. Deneault, D. Bash, F. Mekki-Berrada, S. A. Khan, K. Hippalgaonkar, B. Maruyama, K. A. Brown, J. Fisher III, T. Buonassisi, *npj Comput. Mater.* **2021**, *7*, 188.
[49] J. R. Deneault, J. Chang, J. Myung, D. Hooper, A. Armstrong, M. Pitt, B. Maruyama, *MRS Bull.* **2021**, *46*, 566.
[50] S. Belakaria, A. Deshwal, J. R. Doppa, *Advances in neural information processing systems* **2019**, 32.
[51] K. Qiu, G. Haghiashtiani, M. C. McAlpine, *Annu. Rev. Anal. Chem.* **2018**, *11*, 287.
[52] C. E. Rasmussen, C. K. I. Williams, *Gaussian Processes for Machine Learning*, The MIT Press, Cambridge, MA **2005**.
[53] S. Belakaria, A. Deshwal, J. R. Doppa, *Max-value entropy search for multi-objective Bayesian optimization with constraints*, **2020**.
[54] S. Daulton, D. Eriksson, M. Balandat, E. Bakshy, *Multi-objective bayesian optimization over high-dimensional search spaces. in Uncertainty in Artificial Intelligence, PMLR* **2022**, *180*, 507
[55] S. Belakaria, A. Deshwal, N. K. Jayakodi, J. R. Doppa, in Proceedings of the AAAI Conference on Artificial Intelligence. **2020**, *34*, 10044.
[56] S. Daulton, M. Balandat, E. Bakshy, *Adv. Neural Infor. Process. Sys.* **2020**, *33*, 9851.
[57] J. Mockus, V. Tiesis, A. Zilinskas, *Towards Global Optimization* **1998**, *2*, 117.
[58] N. Srinivas, A. Krause, S. M. Kakade, M. Seeger, *Comp. Sci.* **2009**.
[59] W. R. Thompson, *Biometrika* **1933**, *25*, 285.
[60] E. Zitzler, L. Thiele, *IEEE Transactions on Evolutionary Computation* **1999**, *3*, 257.
[61] Z. Li, T. Muller, A. Evans, R. H. Taylor, M. Unberath, M.-Y. Liu, C.-H. Lin, in *Proceedings of the IEEE/CVF Conference on Computer Vision and Pattern Recognition*. **2023**.